Supplementary Information: Nanomechanical Spectroscopy of 2D Materials

Jan N. Kirchhof[1]*, Yuefeng Yu[1], Gabriel Antheaume[1], Georgy Goardeev[1], Denis Yagodkin[1], Peter Elliott[2], Sangeeta Sharma[2], Stephanie Reich[1] and Kirill I. Bolotin[1]*

[1] Department of Physics, Freie Universität Berlin, Arnimallee 14, 14195 Berlin, Germany

[2] Max-Born Institute for Nonlinear Optics and Short Pulse Spectroscopy,

Max-Born-Strasse 2A, 12489 Berlin Germany

*jan.kirchhof@fu-berlin.de   *kirill.bolotin@fu-berlin.de

1. <u>Finite element method (FEM) simulations</u>

For the FEM modelling we use the structural mechanics module of COMSOL Multiphysics Version 5.5. We build a model around the suspended area partially including the silicon support (Fig. S1a) and use a swept mesh for the thin layers with high density around for TMD flake and SiN window (Fig. S1b). To determine the resonance frequency and mode shape (Fig. S1c) we conduct a prestressed eigenfrequency study. To include the effect of laser heating, we add a study step to implement a Gaussian heat source (Fig. S1d, 30.4% absorption and 30 µW laser power – comp. Fig. 3a main paper) and calculate the heat profile upon laser heating of the center of the suspended TMD (Fig. S1e). This allows us to determine the conversion factor, which captures the tuning of the fundamental mode with laser power, following Eq. 1 from the main paper. The conversion factor slightly depends on wavelength of the heating laser because the laser spot size varies with wavelength, what results in a slightly different heat profile in the suspended TMD. To account for this, we measure the spot size of heating laser at different wavelengths and use this as input for our simulations. In Fig. S1f we plot the conversion factor for device #1 (3L WSe_2). For device #2 (4L MoS_2), we obtain a conversion factor in the range of 461 to 476 Hz/µW showing comparable scaling with wavelength as device #1. The difference between devices here is due to different thermal conductivities, hole sizes and layer thickness between devices.
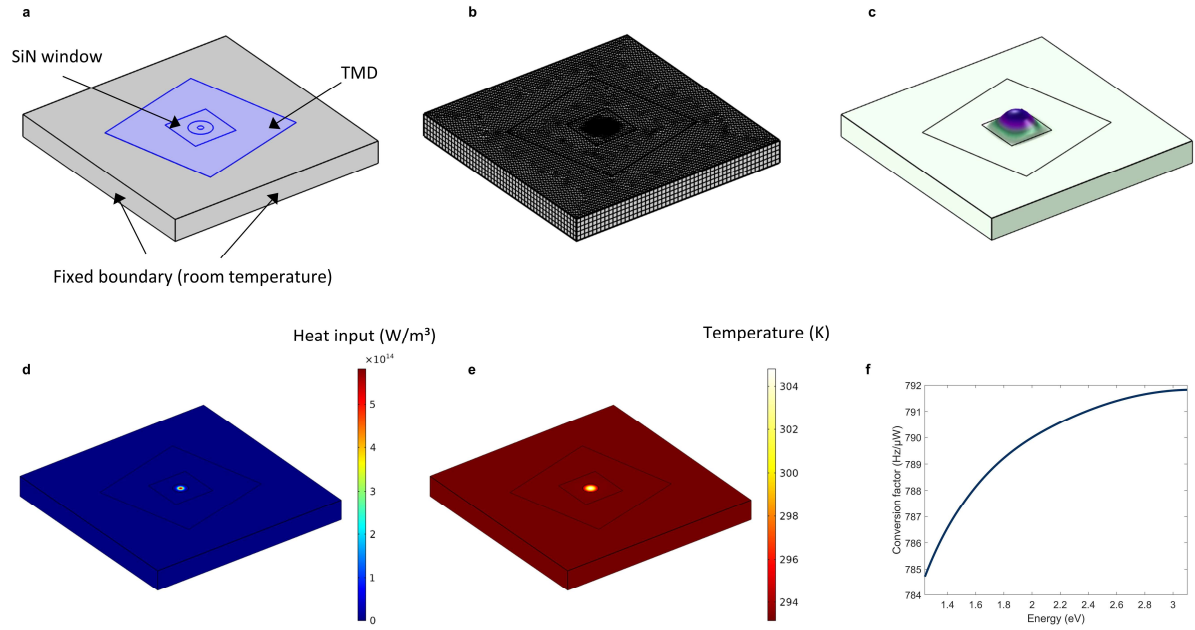
Figure S1 FEM simulations of SiN-TMD hybrid devices a) Model geometry with a thin layer of TMD (blue) placed on the SiN window **b)** Corresponding mesh, all thin layers are meshed as swept layers with high density **c)** Simulated fundamental mode of the hybrid system **d)** Heat input in the shape of a gaussian beam to simulate the effect of laser heating **e)** Resulting heat profile upon 30 μW incident laser power and 30.4 % absorption (corresponds to a photon energy of 2.92 eV for the 3L WSe_2 sample) **f)** Obtained conversion factor for Device #1 (3L WSe_2).

In order to optimize the dimensions of the SiN window, we simulate the driven mechanical resonances in the frequency domain. We start by simulating a circular TMD-only drum resonator (diameter 10 μm) as reference and adjust the isotropic damping to match the experimental Q for such resonators (~100). We then simulate the entire hybrid device (including SiN and gold). In Fig. S2a we plot the simulated displacement vs. frequency for the hybrid device probed on the SiN area, 2 μm away from the suspended TMD area. Again, we adjust the isotropic damping in SiN and gold to match experimental values. We now vary the SiN window size and extract the amplitude of motion at constant drive (signal strength, plotted in Fig. S2b). As expected, larger devices oscillate at large amplitudes providing more signal. Nevertheless, while oscillating at a higher amplitude, larger devices are less responsive to heating. Indeed, in Fig. S2c we plot the relative responsivity (change of resonance frequency for a constant laser heating) vs. window size. Combining the insights from Fig. S2b,c we choose a window size of 20 μm as a reasonable compromise between high vibrational amplitude and high responsivity.
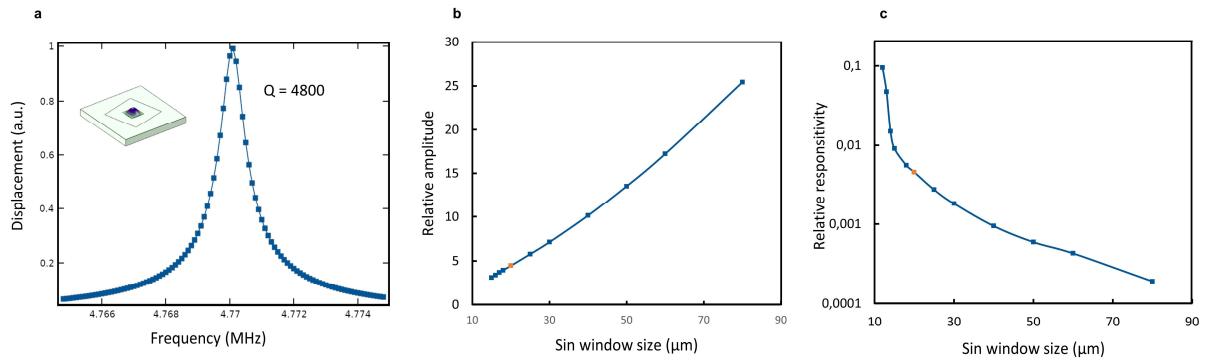
Figure S2 Finding ideal device parameters a) Simulated mechanical motion of the hydride with Q matching experimental results **b)** Simulated amplitude (signal strength) vs. SiN window size **b)** Relative responsivity to laser heating vs. SiN window size. We choose a window size of 20 μm (orange spot) as a compromise between high responsivity and sufficient amplitude amplification

All material properties used in our simulations are summarized in table 1. For quantities that show a large spread in the literature values (values for the TMD materials in particular) we used average values. In general, we preferably choose experimental references for suspended samples of the suitable layer thickness.

Material	Quantity	Value	Reference
MoS_2	Young's modulus E	330 GPa	[1] in agreement with our AFM force-indentation measurements.
	Poisson's ratio ν	0.125	[1]
	Density ρ	5060 kg/m³	[2]
	Thermal conductivity κ	60.3 W/(m·K)	[3–6]
	Thermal expansion coefficient α	$7.6 \cdot 10^{-6}$ 1/K	[7] [8]
	Heat capacity at constant pressure c_p	397 J/(kg·K))	[9,10]
	Built-in tension σ_0	44.7 MPa = 0.11 N/m	Force-indetantion AFM
	Layer thickness d	0.615 nm	[11]

4

WSe$_2$	Young's modulus E	167.3 GPa	[12] In agreement with our AFM force-indentation measurements (shown below)
	Poisson's ratio ν	0.19	[13]
	Density ρ	9320 kg/m³	[14]
	Thermal conductivity κ	26.5 W/(m·K)	[15]
	Thermal expansion coefficient α	$7 \cdot 10^{-6}$ 1/K	[7]
	Heat capacity at constant pressure c_p	188 J/(kg·K)	[9]
	Built-in tension σ_0	46.2 MPa = 0.09 N/m	AFM force indentation
	Layer thickness d	0.651 nm	[11]
Au	Young's modulus E	78.5 GPa	[16]
	Poisson's ratio ν	0.42	[16]
	Density ρ	19300 kg/m³	[16]
	Thermal conductivity κ	312 W/(m·K)	[16]
	Thermal expansion coefficient α	$14 \cdot 10^{-6}$ 1/K	[16]
	Heat capacity at constant pressure c_p	130 J/(kg·K)	[16]
	Pre-stress	160 MPa	[17]
SiN	Young's modulus E	232 GPa	[18]
	Poisson's ratio ν	0.23	[18]
	Density ρ	2810 kg/m³	[19]
	Thermal conductivity κ	31 W/(m·K)	[18]
	Thermal expansion coefficient α	$2.55 \cdot 10^{-6}$ 1/K	[18]
	Heat capacity at constant pressure c_p	887 J/(kg·K)	[18]
	Pre-stress	240 MPa	Norcada (manufacturer)

Si	Young's modulus E	160 GPa	[20]
	Poisson's ratio ν	0.27	[20]
	Density ρ	2330 kg/m³	[20]
	Thermal conductivity κ	160 W/(m·K)	[20]
	Thermal expansion coefficient α	$3 \cdot 10^{-6}$ 1/K	[20]
	Heat capacity at constant pressure c_p	692 J/(kg·K)	[20]
	Pretension	0	Irrelevant for simulations

2. AFM force indentation

One crucial parameter, which is known to vary from device to device is the built-in tension and 2D elastic modulus. To eliminate this uncertainty in our simulations, we perform force indentation measurements in the centre of the membrane (following Ref. [21]) and extract the built-in tension and 2D elastic modulus for each sample. We use cantilevers of intermediate stiffness (k~3 N/m) and only apply small loads (150 nN) to avoid damaging the sample. In Fig. S3a we show a force-displacement-curve for device #1. We account for cantilever bending and deformation of the SiN membrane. We fit a curve following:

$$F = \pi\sigma d + q^3 \frac{E_{2D}}{a^2} d^3 \qquad\qquad \text{(S1)}$$

Here a is the radius of the drum, and $q = \frac{1}{1.05 - 0.15\nu - 0.16\nu^2}$ is a dimensional factor dependent on the Poisson's ratio ν ($q = 0.98$ for WSe$_2$ and q = 0.97 for MoS$_2$). For a range of samples, we find a linear dependence on tension with layer thickness (Fig. S3b). We attribute the observed homogeneity to the cleanliness and uniformity in our samples after annealing (comp. Fig. S4).
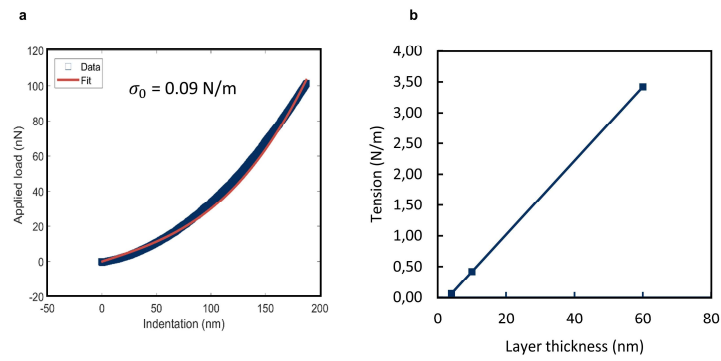
Figure S3 AFM force indentation to determine pre-tension. a) Force vs. displacement as well as a fit to Eq. S1. We extract a pretension of roughly 0.1 N/m for most our devices **b)** Statistics on pre-tension vs. thickness. We find a linear relation between pre-tension and layer thickness in our devices.

3. <u>Sample overview</u>

We fabricate and measure multiple samples. Microscope images and AFM topography scans for device #1-3 are shown in Fig. S4a,b,d,e,g,h. For all samples (Fig. S4c,f,i), we find a high Q fundamental mode of almost constant (except device #3, which has a thicker gold layer). There are some variations in frequency, because the hole size and gold thickness are different for the devices. Our simulations (grey dashed lines) describe the measured frequencies well (Fig. S4c,f,i).
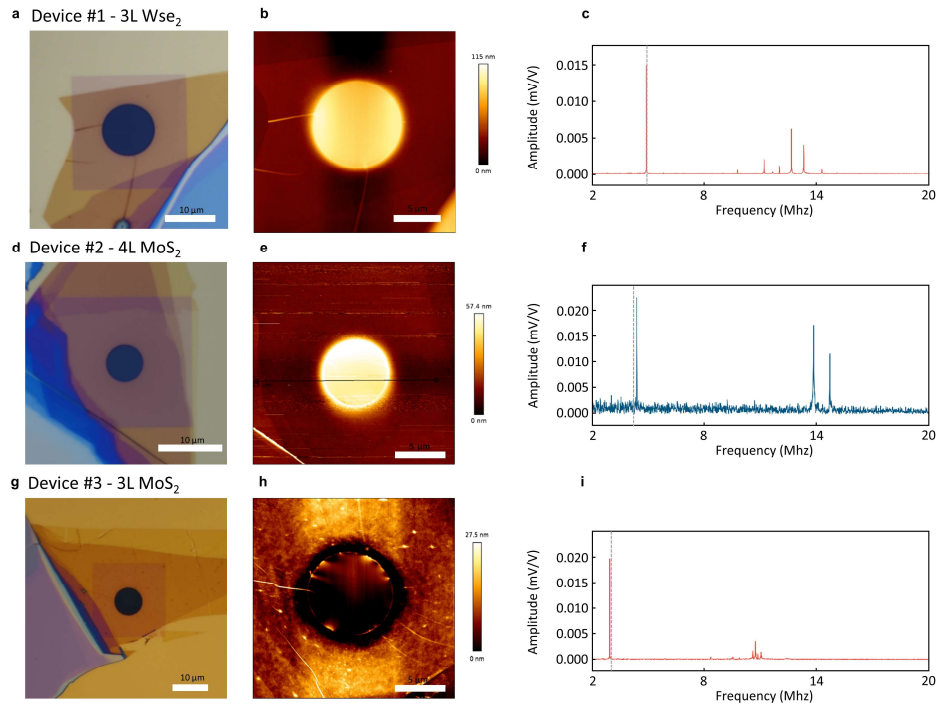
Figure S4 Sample overview. Microscope images **(a,d,g)** and AFM topography **(b,e,h)** of device #1-3. The samples are uniform and well attached to the substrate **c,f,i)** Displacement (amplitude) vs. frequency for device #1-3. We find a dominant high-Q fundamental mode for all samples. The resonance frequencies match with simulated values (grey dashed lines).

4. Details on interferometric motion detection

The interferometric setup is shown in detail in Fig. S5a. Along the beam path of the probe laser, we first implement an optical isolator to avoid back reflected light into the laser, which can cause instabilities and power fluctuations. The beam is then expanded to completely fill the objective (40x 0.6NA). In a first beam splitter we add light from the excitation laser and in a second beam splitter, we guide half the light towards the reference arm and half through the objective onto the sample in a vacuum chamber. The relative position of the reference arm to the sample determines the amplitude of the interferometric signal. We use a piezo electric element to control this distance and stabilize the system using a PID-loop locked to a small reference signal at 941 Hz sourced by Lock-In amplifier (Zurich Instruments MLFI). The sample in the vacuum chamber is clamped upside down onto our sample holder and with a spacing of roughly 40 µm, we place our grounded gate electrode. Electrical driving is realized by mixing a DC voltage (210 V, supplied by a Keithley source meter) with an AC component (typically -5 dBm) from our vector network analyzer (VNA, Agilent E5071C) in a high

voltage Bias T (Particulars BT-01) and applying it to the gold layer of the sample, which contacts the TMD flake. For smaller frequency ranges and phase-locked-loop (PLL) measurement, we use a lock-in amplifier (Zurich Instruments MFLI). In Fig. S5b we show the power spectra of our excitation laser source (measured at the sample position) with different neutral density filters (ND) implemented, which are used to calculate the relative frequency shifts $\frac{\Delta f}{\Delta P}$. We perform a small linear correction (order of Hz) to account for temperature changes in the room during measurements of the maps (Fig. 2 a,c). In the PLL-configuration (25 kHz bandwidth) we can measure the heating induced frequency shifts Δf quickly and with high sensitivity even at low laser powers (raw data for ND 1.5 in Fig. S5c).
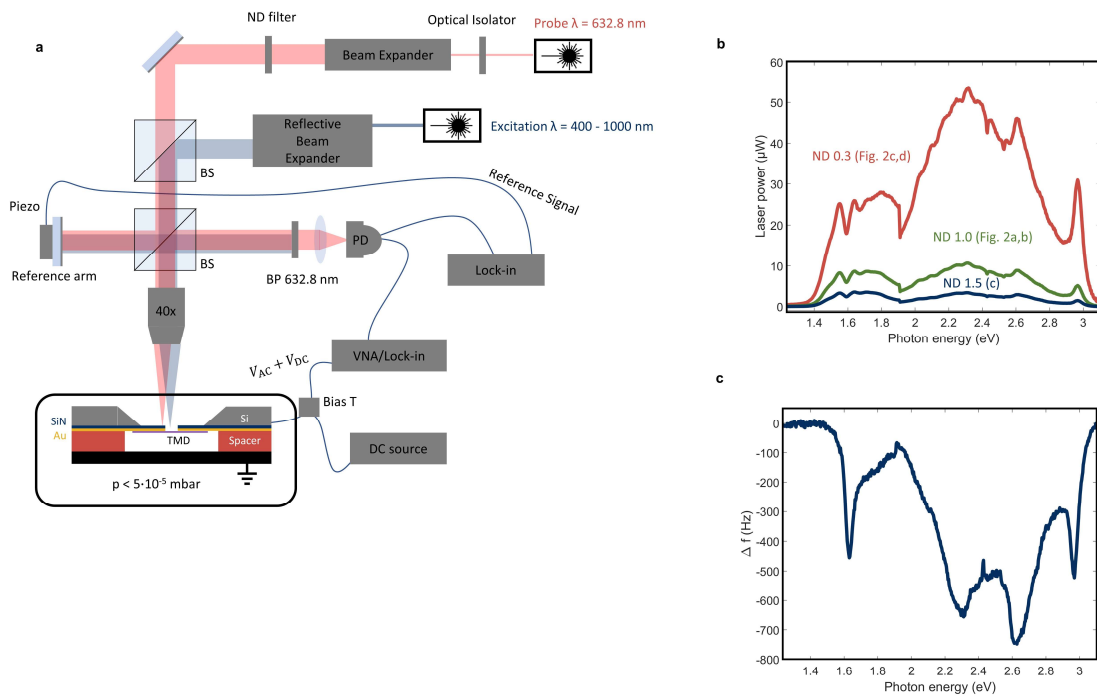
Figure S5 Setup details and PLL-data a) Detailed sketch of setup and **b)** Measured output of the tunable excitation laser at the sample position vs. wavelength. This data is used to normalize the frequency shift. **c)** PLL measurements of device #1, using the laser power plotted in **b)**.

5. <u>Consideration of dynamical back-action effects</u>

In nanomechanical resonators also dynamic optomechanical back-action (in contrast to static heating) effects can alter the resonance frequency (f) and its FWHM (f_{FWHM}) especially at large laser powers.[22–24] This occurs e.g. in cavity interferometers, where the laser power, which the oscillating membrane is exposed to, varies significantly over a short spatial distance.[22,23] For this a reflective surface close to the moving membrane is needed.[22,23] The effects furthermore only occur when the

spatial symmetry is broken due to deforming the membrane out of plane.[22,23] In our system the gate is non-reflective and far away from the membrane (~ 40 µm). Additionally, the applied electrostatic pressure by the gate voltage is relatively small and SiN-TMD hybrid system rather stiff, so there is no breaking of symmetry in out of plane direction. Considering all the points above, we can exclude cavity related back-action effects in our system.

Also, strain-induced shifts in absorption in the material itself can cause dynamic back-action effects.[24] Here again a breaking of symmetry, large laser powers and soft systems (small spring constant) are needed. We therefore also exclude material related back-action effects.

To verify this experimentally we extract f_{FWHM}, whilst illuminating the sample at different wavelengths (Fig. S6a,b). If there were any dynamic back-action effects influencing the system, the f_{FWHM} should show significant variations.[22–24] We do not observe such variations and thereby experimentally confirm the absence of dynamic back-action effects.
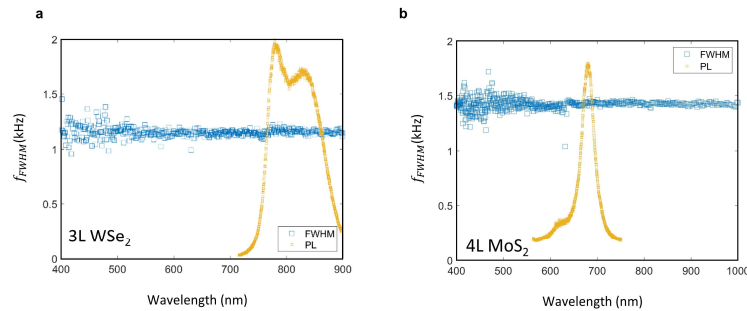
Figure S6 Reference measurements check for dynamic back-action effects. a,b) FWHM vs. wavelength for device #1 (WSe$_2$) and #2 (MoS$_2$) and photoluminescence measurements as reference for the excitonic resonances. We observe a constant FWHM over the entire wavelength range and thereby experimentally exclude dynamic optomechanical back action effects.

6. Laser induced frequency shifting (derivation of Eq.1)

We model the TMD-SiN-hybrid device as two 1D-springs in series, one representing the suspended TMD area and another the SiN window. The total spring constant is then given by:

$$k_{total} = \frac{1}{\frac{1}{k_{SiN}} + \frac{1}{k_{TMD}}} \qquad (S2)$$

The fundamental resonance frequency of the system is then:

$$f_0 = \frac{1}{\sqrt{m_{eff}}} \frac{1}{\sqrt{\frac{1}{k_{SiN}} + \frac{1}{k_{TMD}})}}, \qquad (S3)$$

where m_{eff} denotes the effective mass of the mode. With the heating laser turned on, light is absorbed and the TMD area heats up and thus k_{TMD} gets reduced by Δk. The resonances frequency with laser heating can be expressed as:

$$f(k_{TMD} - \Delta k) = \frac{1}{\sqrt{m_{eff}}} \frac{1}{\sqrt{\frac{1}{k_{SiN}} + \frac{1}{k_{TMD}(1 - \frac{\Delta k}{k_{TMD}})}}} \qquad (S4)$$

We now expand the term to first order for $\frac{\Delta k}{k_{TMD}} \ll 1$ and obtain

$$f(k_{TMD} - \Delta k) \approx f_0 - \frac{1}{\sqrt{m_{eff}}} \frac{\left(\frac{k_{SiN} k_{TMD}}{k_{SiN} + k_{TMD}}\right)^{\frac{3}{2}}}{2 k_{SiN}} \frac{\Delta k}{k_{TMD}} \qquad (S5)$$

We subtract f_0, and obtain the frequency shift induced upon laser heating $\Delta f = f(k_{TMD} - \Delta k) - f_0$:

$$\Delta f = \frac{1}{\sqrt{m_{eff}}} \frac{\left(\frac{k_{SiN} k_{TMD}}{k_{TMD} + k_{SiN}}\right)^{\frac{3}{2}}}{2 k_{SiN}} \frac{\Delta k}{k_{TMD}} \qquad (S6)$$

For the "TMD-spring", we can relate the change in spring constant to a change in built-in tension:

$$\frac{\Delta k}{k_{TMD}} = \frac{\Delta \sigma}{\sigma_0} \qquad (S7)$$

The change in tension due to thermal expansion is given by:

$$\Delta \sigma = \frac{\alpha E_{2D}}{1 - \nu} \Delta T, \qquad (S8)$$

Where α is the thermal expansion coefficient, E_{2D} is the 2D elastic modulus and ν is the Poisson's ratio of the TMD. The change in temperature ΔT is proportional to the amount of absorbed laser power:

$$\Delta T = \frac{\beta Abs(\lambda)}{h\kappa} \Delta P, \qquad (S9)$$

11

where κ is the thermal conductivity, h is the thickness of the membrane and β is a pre-factor determined by the temperature profile in the membrane. Combining Eq. S6-9 we obtain Eq. 1 from the main text:

$$\frac{\Delta f}{\Delta P}(\lambda) = \frac{1}{\sqrt{m_{eff}}} \frac{\left(\frac{k_{SiN}k_{TMD}}{k_{TMD}+k_{SiN}}\right)^{\frac{3}{2}}}{2k_{SiN}} \frac{\beta}{2h\kappa} \frac{\alpha E_{2D}}{\sigma_0(1-\nu)} Abs(\lambda), \qquad (S10)$$

7. Reflection measurements

The setup presented in the main text also allows us to perform reflection measurements. We block the reference arm, turn off the probe laser and then and use our tunable excitation light source to sweep the wavelength whilst recording the reflected signal off our sample using a chopper (920Hz) and the lock-in amplifier (Fig. S7a, green). We then subtract spectra from that from an empty hole as shown in Fig. S8a (Fig. S7a, blue) and normalize the data by dividing by a "100% reflection reference", which we obtain measuring reflection of a silver mirror (Fig. S7a, red) with known reflection properties (Thorlabs PF10-03-P01). The resulting reflection data is shown in Fig. S7b.
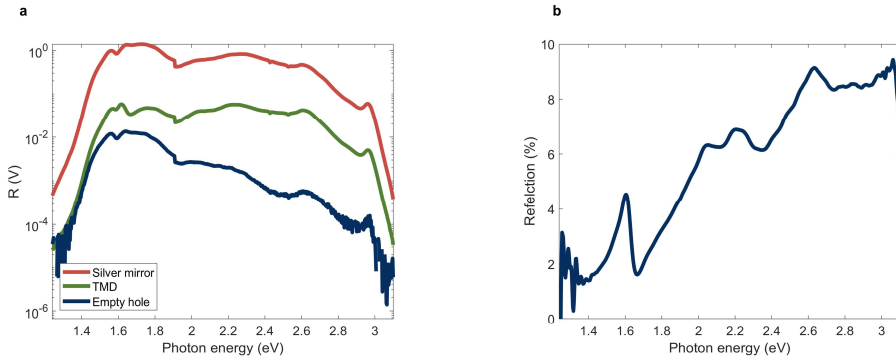
Figure S7 Optical reflection measurements a) Reflection of device #1 (3L WSe$_2$), a silver mirror, corresponding to our 100% reflection reference and an empty hole **b)** Resulting reflection data for the TMD material.

8. Obtaining the dielectric function

Reflection and transmission of electromagnetic waves was computed with the transfer matrix formalism. Two types of matrices are required: a propagation matrix P and a boundary matrix T. The propagation matrix contains elements responsible for phase change inside a material

$$P(\lambda, n, d) = \begin{pmatrix} e^{2\pi i n d/\lambda} & 0 \\ 0 & e^{-2\pi i n \, /\lambda} \end{pmatrix}, \qquad \text{(S11)}$$

where n is complex refractive index of the material, λ wavelength of light, d is the thickness of the material. Whereas the boundary matrix depends on the refractive indices on both sides of the boundary n_1 and n_2:

$$T(n_1, n_2) = \frac{1}{t_{12}} \begin{pmatrix} 1 & r_{12} \\ r_{12} & 1 \end{pmatrix}. \qquad \text{(S12)}$$

The $t_{12} = \frac{2n_1}{n_1 + n_2}$ is a Frensel transmission coefficient for oblique incidence and the r_{12} is a reflection coefficient $\frac{n_1 - n_2}{n_1 + n_2}$. The overall transfer matrix M of vacuum suspended TMDC yields

$$M = T(n_{vacuum}, n_{TMDC}) \cdot P(\lambda, n_{TMDC}, d) \cdot T(n_{TMDC}, n_{vacuum}). \qquad \text{(S13)}$$

For each wavelength, we compute the refractive index $n_{TMDC} = n + Ik$ using matrix elements. The system of two equations is solved for two variables n, k.

$$\begin{cases} Trans = 1 - Abs - Refl = 1/|M_{11}|^2 \\ \qquad Refl = |M_{21}|^2 / |M_{11}|^2 \end{cases}, \qquad \text{(S14)}$$

$Abs, Refl$ are experimentally obtained absorption and reflection, respectively. The dielectric function ε is obtained using relation $\varepsilon = n^2$.

9. RPA and BSE calculations

To determine the theoretical response function the ground-state of the material was first calculated using density functional theory (DFT). Within DFT, the exchange-correlation energy was approximated by the local density approximation (LDA), which is well known for underestimating the bandgap of insulators and semiconductors. In order to estimate the experimental direct bandgap G_0W_0 calculations[25] were performed and the DFT band-structure was then corrected by the scissor operator to obtain the correct direct bandgap.

This corrected band-structure was then used to determine the response function of the material. In order to account for excitonic effects the Bethe Salpeter equation (BSE) was solved[26]. Solving the BSE is computationally very demanding and hence the BSE Hamiltonian was diagonalized in a restricted active space of a few bands around the Fermi level. However, the consequence of this restriction is that the response function is only determined in a limited low energy window around the band-gap. In order to obtain the response function at higher energies, where excitonic effects are negligible, we use the so-called random-phase approximation (RPA) within linear response time-dependent density functional theory (TDDFT).[27,28] This procedure does not account for excitonic effects, but bands up to 100 eV above the Fermi energy are included and is an accurate method for determination of response function away from the band-gap energies.

Computational parameters: Spin-orbit coupling was included for all calculations. For the DFT calculations the in-plane lattice parameter for WSe_2 (MoS_2) was 3.28 Å (3.16 Å) with an interlayer spacing of 6.48 Å (6.15 Å), a distance of 3.34 Å (3.17 Å) between the chalcogens in each layer, and vacuum spacing between top and bottom layers of at least 12 Å for both the tri- and tetra-layer calculations. A k-point grid of 30x30x1 was used in all cases. The BSE hamiltonian was diagonalized in the restricted active space of 8 valence and 8 conduction states around the Fermi level. In order to account for many-body effects we have performed a single shot, finite temperature (a temperature of 500 K was used), all electron, spin-polarized GW calculations, where the spectral function on the real axis is constructed using a Pade approximation. Spin-orbit coupling was included in the GW calculations and a Matsubara cut-off of 12 Ha was used. All calculations were performed using state-of-the-art, all-electron, full-potential code Elk.[29]

10. Determination of sensitivity via Allan deviation:

The Allan deviation is defined as:[30]

$$\sigma_A^2(t) = \frac{1}{2(N-1)f_0^2}\sum_{i=2}^{N}(f_i - f_{i-1})^2 \qquad (S15)$$

where f_i is the average frequency measured over the ith time interval of length t. We perform time stability measurements (Fig. 5b, main paper) of the resonance frequency with the heating laser turned

off using a PLL with a bandwidth BW = 2.5 kHz. We extract σ_A and find $\sigma_A < 5\cdot10^{-7}$ over a broad range

(Fig. 5c, main paper). Plugging $\frac{\Delta f}{\Delta P} = 792$ Hz/µW, $f_0 = 4.6702$ MHz and an optimal $\sigma_A = 2.426 \cdot10^{-7}$

at a sampling period of $t = 4$ ms into equation S16, we calculate $= 90 \frac{pW}{\sqrt{Hz}}$. The measurement fulfils

the condition of $t \gg \frac{1}{BW}$.

$$\eta = \frac{\sigma_f\sqrt{t}}{f_0\left(\frac{\Delta f}{f_0\Delta P}\right)} = \frac{\sigma_A\sqrt{t}f_0}{\frac{\Delta f}{\Delta P}}, \qquad\qquad \text{(S16)}$$

References

(1)   Castellanos-Gomez, A.; Poot, M.; Steele, G. A.; Van Der Zant, H. S. J.; Agraït, N.; Rubio-Bollinger, G. Elastic Properties of Freely Suspended MoS2 Nanosheets. *Adv. Mater.* **2012**, *24* (6), 772–775.

(2)   GESTIS-Stoffdatenbank https://gestis.dguv.de/data?name=570192 (accessed Jan 24, 2022).

(3)   Sahoo, S.; Gaur, A. P. S.; Ahmadi, M.; Guinel, M. J. F.; Katiyar, R. S. Temperature-Dependent Raman Studies and Thermal Conductivity of Few-Layer MoS2. *J. Phys. Chem. C* **2013**, *117* (17), 9042–9047.

(4)   Zhang, X.; Sun, D.; Li, Y.; Lee, G. H.; Cui, X.; Chenet, D.; You, Y.; Heinz, T. F.; Hone, J. C. Measurement of Lateral and Interfacial Thermal Conductivity of Single- and Bilayer MoS2 and MoSe2 Using Refined Optothermal Raman Technique. *ACS Appl. Mater. Interfaces* **2015**, *7* (46), 25923–25929.

(5)   Aiyiti, A.; Bai, X.; Wu, J.; Xu, X.; Li, B. Measuring the Thermal Conductivity and Interfacial Thermal Resistance of Suspended MoS2 Using Electron Beam Self-Heating Technique. *Sci. Bull.* **2018**, *63* (7), 452–458.

(6)   Yuan, P.; Wang, R.; Wang, T.; Wang, X.; Xie, Y. Nonmonotonic Thickness-Dependence of in-Plane Thermal Conductivity of Few-Layered MoS2: 2.4 to 37.8 Nm. *Phys. Chem. Chem. Phys.* **2018**, *20* (40), 25752–25761.

(7)   ÇakIr, D.; Peeters, F. M.; Sevik, C. Mechanical and Thermal Properties of h -MX2 (M = Cr, Mo, W; X = O, S, Se, Te) Monolayers: A Comparative Study. *Appl. Phys. Lett.* **2014**, *104* (20), 203110.

(8)   Zhang, L.; Lu, Z.; Song, Y.; Zhao, L.; Bhatia, B.; Bagnall, K. R.; Wang, E. N. Thermal Expansion Coefficient of Monolayer Molybdenum Disulfide Using Micro-Raman Spectroscopy. *Nano Lett.* **2019**, *19* (7), 4745–4751.

(9)   Min, K.-A.; Cha, J.; Cho, K.; -, al; Jin Yun, S.; Hoon Jung, K.; Hyun Kim -, S.; Lee, J.; Huang, J.; Nakamura, K. First-Principles Simulation on Thermoelectric Propertiesof Transition Metal Dichalcogenide Monolayers. *Japanese J. Appl. Phys. Regul. Pap.* **2018**, *57*, 6–10.

(10)   Volovik, L. S.; Fesenko, V. V.; Bolgar, A. S.; Drozdova, S. V.; Klochkov, L. A.; Primachenko, V. F. Enthalpy and Heat Capacity of Molybdenum Disulfide. *Sov. Powder Metall. Met. Ceram.* **1978**, *17* (9), 697–702.

(11)   Xu, J.; Zhang, J.; Zhang, W.; Lee, C. S. Interlayer Nanoarchitectonics of Two-Dimensional Transition-Metal Dichalcogenides Nanosheets for Energy Storage and Conversion Applications. *Advanced Energy Materials*. John Wiley & Sons, Ltd December 1, 2017, p 1700571.

(12)   Zhang, R.; Koutsos, V.; Cheung, R. Elastic Properties of Suspended Multilayer WSe2. *Appl. Phys. Lett.* **2016**, *108* (4).

(13)   Kang, J.; Tongay, S.; Zhou, J.; Li, J.; Wu, J. Band Offsets and Heterostructures of Two-Dimensional Semiconductors. *Appl. Phys. Lett.* **2013**, *102* (1), 012111.

(14)   Agarwal, M. K.; Wani, P. A. Growth Conditions and Crystal Structure Parameters of Layer Compounds in the Series Mo1-XWxSe2. *Mater. Res. Bull.* **1979**, *14* (6), 825–830.

(15)   Easy, E.; Gao, Y.; Wang, Y.; Yan, D.; Goushehgir, S. M.; Yang, E. H.; Xu, B.; Zhang, X. Experimental and Computational Investigation of Layer-Dependent Thermal Conductivities and Interfacial Thermal Conductance of One- To Three-Layer WSe2. *ACS Appl. Mater. Interfaces* **2021**, *13* (11), 13063–13071.

(16)   AZoM. Gold - Properties and Applications of Gold. *AZO Materials*. 2001, pp 1–3.

(17)   Wilcock, J. D.; Campbell, D. S.; Anderson, J. C. The Internal Stress in Evaporated Silver and Gold Films. *Thin Solid Films* **1969**, *3* (1), 13–34.

(18)   Properties: Silicon Nitride (Si3N4) Properties and Applications https://www.azom.com/properties.aspx?ArticleID=53 (accessed Jan 24, 2022).

(19)   Huszank, R.; Csedreki, L.; Kertész, Z.; Török, Z. Determination of the Density of Silicon–Nitride Thin Films by Ion-Beam Analytical Techniques (RBS, PIXE, STIM). *J. Radioanal. Nucl. Chem.* **2016**, *307* (1), 341–346.

(20)   Properties: Supplier Data - Silicon (Si) https://www.azom.com/properties.aspx?ArticleID=1851 (accessed Jan 24, 2022).

(21)   Lee, C.; Wei, X.; Kysar, J. W.; Hone, J. Measurement of the Elastic Properties and Intrinsic Strength of Monolayer Graphene. *Science (80-.).* **2008**, *321* (5887), 385–388.

(22)   Barton, R. A.; Storch, I. R.; Adiga, V. P.; Sakakibara, R.; Cipriany, B. R.; Ilic, B.; Wang, S. P.; Ong, P.; McEuen, P. L.; Parpia, J. M.; Craighead, H. G. Photothermal Self-Oscillation and Laser Cooling of Graphene Optomechanical Systems. *Nano Lett.* **2012**, *12* (9), 4681–4686.

(23)   Morell, N.; Tepsic, S.; Reserbat-Plantey, A.; Cepellotti, A.; Manca, M.; Epstein, I.; Isacsson, A.; Marie, X.; Mauri, F.; Bachtold, A. Optomechanical Measurement of Thermal Transport in Two-Dimensional MoSe 2 Lattices. *Nano Lett.* **2019**, *19* (5), 3143–3150.

(24)   Xie, H.; Jiang, S.; Rhodes, D. A.; Hone, J. C.; Shan, J.; Mak, K. F. Tunable Exciton-Optomechanical Coupling in Suspended Monolayer MoSe2. *Nano Lett.* **2021**, *21* (6), 2538–2543.

(25)   Kim, H. G.; Choi, H. J. Thickness Dependence of Work Function, Ionization Energy, and Electron Affinity of Mo and W Dichalcogenides from DFT and GW Calculations. *Phys. Rev. B* **2021**, *103* (8), 085404.

(26)   Salpeter, E. E.; Bethe, H. A. A Relativistic Equation for Bound-State Problems. *Phys. Rev.* **1951**, *84* (6), 1232–1242.

(27)   Runge, E.; Gross, E. K. U. Density-Functional Theory for Time-Dependent Systems. *Phys. Rev. Lett.* **1984**, *52* (12), 997–1000.

(28)   Sharma, S.; Dewhurst, J. K.; Gross, E. Optical Response of Extended Systems Using Time-Dependent Density Functional Theory. *Top. Curr. Chem.* **2014**, *347*, 235–258.

(29)   The Elk Code https://elk.sourceforge.io/ (accessed Jan 24, 2022).

(30)   Allan, D. W. Statistics of Atomic Frequency Standards. *Proc. IEEE* **1966**, *54* (2), 221–

230.